Optimization of Three-Dimensional-Printed Catalytic Electrodes for Alkaline Water Electrolysis Guided by the Experimental Design Methodology

Jeoffrey Tourneur, Loïc Perrin, Stéphane Paul, Bruno Fabre

Optimization of 3D-Printed Catalytic Electrodes for Alkaline Water Electrolysis Guided by the Experimental Design Methodology

Jeoffrey Tourneur[1,2], Loïc Perrin[2,*], Stéphane Paul[2], and Bruno Fabre[1,*]

[1] Jeoffrey Tourneur and Bruno Fabre– CNRS, ISCR (Institut des Sciences Chimiques de Rennes) – UMR6226, Univ Rennes, Rennes F-35000, France.

[2] Jeoffrey Tourneur, Loïc Perrin and Stéphane Paul – SAS H2X Ecosystems - High Park II - 10, rue Louis Blériot, 35170 Bruz, France

KEYWORDS: *Water Splitting, Design of Experiments, Alkaline Electrolysis, 3D Printing, Transition Metal Electrocatalysts*

ABSTRACT: Dihydrogen (H_2) is considered nowadays as a sustainable energy carrier and exhibits a high energy density in its highly compressed state. Different countries in the world are developing its industrial production and are scaling up water electrolysis processes with clear roadmaps. Alkaline water electrolysis is an affordable technology that avoids use of platinum group metals with a good compromise of efficiency because of the development of new cost-effective and Earth-abundant materials of electrodes and new anion exchange membranes. Here, we report on the use of emerging and selective laser melting (SLM) technology for 3D printing of binary alloyed NiFe, NiMo, NiCr, and NiCo electrode materials at an applied scale. These materials are preliminarily tested for hydrogen and oxygen evolution half-reactions in alkaline conditions in order to select the most promising combinations of cathode/anode for overall water electrolysis. Based on three key performance metrics KPMs (namely, overpotential values at 10 and 50 mA cm^{-2}, and the stability in operation over six days at 50 mA cm^{-2}), NiCr and NiCo are preferred for the cathode, whereas the anode is NiMo or NiFe. Moreover, in order to facilitate the release of the electrogenerated gas bubbles, the patterning of 3D-printed electrodes with either roughly-conical holes or ramps is considered as a third experimental factor. The water electrolysis process is then fully optimized by using the formalism of design of experiments (DOE) which allows to reduce the number of experiments without loss in the quality of conclusions. This study reveals that NiCo and NiMo shall be preferentially used as the cathode and anode, respectively, to decrease the cell overvoltage, whereas NiFe as the anode yields the best stability in operation. Besides, the impact of the patterns printed by SLM on the KPMs is somewhat limited, even though the presence of holes is rather beneficial for decreasing cell overvoltage. Interestingly, an approximate calculation of the consumed energy for the production of 1 kg of H_2 from the combination NiCo/NiMo/holes as cathode/anode/pattern yields 50.6 kWh/kg of H_2 which is quite promising if one refers to the 48 kWh industrial target set by European Union for 2030.

1 Introduction.

As the global demand for energy is increasing about 60% from 2010 to 2040[1] when mankind needs to reduce its use of fossil sources of energy[2,3], it becomes crucial to develop new technologies to produce and store energy while reducing greenhouse gas emissions. In that context, dihydrogen $H_{2(g)}$ arouses an increasing interest owing to its high mass energy density (123 MJ kg^{-1}) which can be exploited to produce electricity and heat when consumed in a fuel cell. This flexible and sustainable energy carrier can be produced by the electrolytic water splitting[4–6], which is now widely recognized as a clean and carbon-free route[7]. However, the high cost of water electrolysis is a major barrier to its widespread adoption. This is due in part to the use of scarce and expensive noble metals, such as Pt, Ir, and Ru, as electrode materials. [1,8,9] These metals are principally employed in Proton Exchange Membrane (PEM) electrolysis because of their high catalytic activity and stability in an acidic environment.[12] PEM electrolyzers produce the highest current densities for H_2 production, but they are prone to corrosion due to the harsh oxidizing conditions in the anodic compartment. Therefore, researchers are exploring alternative technologies, such as alkaline water (AWE) and anion exchange membrane (AEM) electrolyzers,[10,11,12] which allow the use of less expensive and more corrosion-resistant transition metals as electrocatalysts for both the hydrogen evolution reaction (HER) and the oxygen evolution reaction (OER).[13,14]

Benchmarking studies by Jaramillo and co-workers have allowed to standardize the electrocatalytic activity for HER and OER in either acid or alkaline conditions of numerous

Ni-based binary or ternary alloys electrodeposited on conductive substrates[15,16]. Alloying metals is a well-known route to tailor the density of states of d electronic band and optimize the electronic structure of the materials to achieve more efficient electrocatalysis[11,17–22]. From now on, states and continental organizations are building plans to develop a hydrogen economy and scale up water electrolysis to an industrial level[2,3,23]. So, in the context of the industrialization of electrode materials, 3D printing appears as an emerging manufacturing technique to decrease operational and capital expenditures of electrodes and electrolysers[24–27]. It allows the fabrication of metallic alloys with tailored compositions, intricate electrode geometries, and porous systems with high resolution and precise control over the surface microstructure. Among the 3D printing methods, Selective Laser Melting (SLM) is particularly powerful to fabricate large metal pieces with original and complex geometries. In SLM, a high-power laser locally melts matter by scanning a metal powder bed in a controlled manner. Pumera's group has recently used this additive manufacturing technique to produce 316L stainless steel 3D printed electrodes for electrochemical energy applications[28–30]. While 3D printing methods have great potential for fabricating practical catalytic electrodes [31], their use to elaborate metallic alloys specifically designed for electrochemical purposes is still underexplored. Inspired by Jaramillo's group works on catalytically active flat electrodes, we have recently printed by SLM 25 cm^2 cylindrical NiFe and NiCo electrodes for efficiently achieving both HER and OER in an alkaline medium[32]. Notably, patterning the electrode surface with cylindrical microstructures was found to be an effective strategy for promoting the release of gas bubbles.

In this work, we extend our contribution to 3D printed NiMo and NiCr binary alloys and propose overall water electrolysis cells incorporating the most promising HER and OER electrode materials which have been optimized using the formalism of design of experiments (DOE). To do this, we employ a 2^3 Hadamard matrix with eight combinations of three experimental factors at two levels to perform an analysis of variance (ANOVA) study and measure linear effects for each factor and interaction between them[33–35]. It is worth emphasizing that the implementation of such a methodology for the design and optimization of water electrolysis cells is unprecedented to the best of our knowledge.

2 Experimental Section.

2.1 Chemicals.

Spherical powders for 3D printing of Ni (purity 99.99 %, 15-35 μm granulometry) were purchased from Hoganas. Spherical powders for 3D printing of Fe, Cr, Mo, and Co (purity 99.99 %, 15-53 μm granulometry) were purchased from Neyco. KOH (>85 %, analysis grade) and absolute ethanol (RSE grade) were purchased from Sigma-Aldrich and Carlo Erbatron, respectively. Ultra-pure water (Veolia Water-STI) with a resistivity of 18.2 MΩ cm was used to prepare the aqueous solutions.

2.2 3D printing.

All electrodes were designed using the software Auto Desk Fusion 360. Magics software was used for implementation on the platform using block and contour supports. A Turbula T2F station was used to mix the atomic powders in a powder bed of NiFe, NiCo, NiMo, or NiCr. Electrodes were produced by SLS France company using the SLM technique in a TechGine TS120 under a nitrogen atmosphere. Each layer of melt metal was 20 μm-thick. The fabricated electrodes were then removed from the support, scraped and sanded, then cleaned under pressurized air. Photographs of the NiMo and NiCr electrodes are shown in Figure S1 (Supporting Information) and those of NiFe and NiCo electrodes are shown in our previous report[32].

2.3 Electrochemistry.

Half-cell configuration. The electrochemical measurements were performed at room temperature on an HTDS PARSTAT PMC-200 multi-channel electrochemical workstation equipped with an AC frequency response analyzer (FRA). The 3D printed electrode was directly used as the working electrode (geometric surface area: 25 cm^2). A graphite rod or a double stabilized anode (DSA, model AO2002, titanium foil covered by mixed ruthenium and iridium oxides, ECS Tarn) was used as the counter electrode for OER or HER, respectively. The reference electrode was either Hg/HgO from Origalys for chronopotentiometry or KCl-saturated Ag/AgCl for cyclic voltammetry. For comparison, a pure Ni electrode (25 cm^2 geometric surface area) was considered. Before use, the working electrode was sonicated for 10 min in ultra-pure water and absolute ethanol to remove the oxide layer and was dried at 70°C for 3 h. An electrical contact was established with an ergot on the electrode and masked with an insulating epoxy resin (Loctite EA9460, Ellswoth Additives). The electrode was then placed into an oven at 90°C overnight to cure the resin.

A homemade H-type electrochemical macrocell with a constant headspace volume was used to carry out long-term electrolytic tests at high current intensities with ca. 25 cm^2 electrodes. The macrocell consisted of two compartments with a total electrolyte capacity of 1.4 L, in order to neglect the volume consumed during the water electrolysis. The headspace volume was 1.25 L per half-cell, so that volume changes caused by the produced gas (H_2 and O_2) could be neglected. This large headspace volume was chosen to avoid overpressure during GC analysis. The cell was sealed by a flat and circular ground joint, closed by a stainless-steel flange. The junction was made by a male-female ground joint sealed with Teflon tape. Septa and epoxy resin (Loctite, EA3423, Ellswoth Additives) were used to seal the openings for gas measurement and introduction of the working electrode.

All cyclic voltammograms (CVs) were recorded at 5 mV s^{-1} and the Ohmic drop was corrected using the cell resistance determined at high frequencies (typically 100 kHz). The corresponding Tafel slopes were determined from the linear overpotential vs. log (current density) (η vs. log j) plots. The current densities were normalized by the geometric surface area of the 3D printed electrodes determined with Auto Desk Fusion 360 software and all the measured potentials were converted versus the reversible hydrogen electrode (RHE) according to the equations given below:

In an alkaline medium (1.0 M KOH, pH = 14 ± 0.1) using a Hg/HgO reference electrode (filled with 0.1 M KOH solution):

$$E_{RHE} = E_{Hg/HgO} + 0.059\ pH + E^0_{Hg/HgO}$$

$$\text{with } E^0_{Hg/HgO} = +0.14\ V \quad (1)$$

In an alkaline medium (1.0 M KOH, pH = 14 ± 0.1) using an Ag/AgCl reference electrode (filled with saturated KCl solution):

$$E_{RHE} = E_{Ag/AgCl} + 0.059\ pH + E^0_{Ag/AgCl}$$

$$\text{with } E^0_{Ag/AgCl} = +0.20\ V \quad (2)$$

where $E_{Hg/HgO}$ and $E_{Ag/AgCl}$ are the applied potential values versus the selected reference electrode. Potentials are given with 5 mV precision and the reference electrodes were controlled every six months[36].

Electrochemical impedance spectroscopy (EIS) measurements were performed at an applied overpotential of 0.1 V for HER and 0.3 V for OER over a frequency range from 100 kHz to 100 mHz (50 frequencies, logarithmic distribution) at 10 mV amplitude. The long-term stability of the catalytic electrodes was examined using chronopotentiometry at an applied ±50 mA cm^{-2} current density. EIS data were analyzed using the Zview software.

Full cell configuration. The electrochemical measurements were performed at room temperature using the same electrochemical workstation and macrocell as those used for the half cell. A two-electrode configuration was used with the 3D printed electrodes (geometric surface area: 25 cm^2) as the cathode and the anode. The electrochemical conditions were identical to those mentioned for the half-cell. Each experimental run was repeated twice so that the DOE theory could be confidently applicable.

2.4 Characterizations

Scanning electron microscopy (SEM) images and EDS (Energy Dispersive X-Ray Spectroscopy) elemental mapping were performed using an IT-300 JEOL microscope and an X-Max 50 mm2 EDS detector (Oxford Instruments).

Profilometry measurements were performed using a Bruker Dektak X profilometer with a Stylus B type tip (12.5 µm curvature radius) and tilt angle correction.

ICP-AES (Inductive Coupled Plasma Atomic Emission Spectroscopy) measurements were performed using a 725 ES Varian station with an argon plasma.

Gas chromatography (GC) measurements for the detection and quantification of the gases produced by electrolysis were performed with a micro-GC Agilent 990 equipped with a TCD detector. The column was heated at 145°C, the injector at 90°C, with Alphagaz 2 Smartop argon (Air Liquide) as the carrier gas at 29 psi. The sampling time was 50 ms and the results are obtained in vol. %. For the determination of the Faradaic efficiency (FE), the apparatus was calibrated with a gas mixture containing N_2 (3%, v/v), CH_4 (5%, v/v), CO (10%, v/v), H_2 (10%, v/v), CO_2 (20%, v/v) and He (52%, v/v) (from GazDetect, UN1954) and air from the laboratory. A H-type cell perfectly closed was used and degassed under Ar for 10 min prior to analysis. A current density of ±10 mA cm^{-2} was applied during 1.5 h and one measurement was realized every 10 min. The current density was selected considering the theoretical gas production to not exceed 10% of the headspace volume of the cell. The FE was determined using the gas perfect law and the pressure value measured by a Vernier sensor. It was expressed versus a reference material (Pt for HER and DSA for OER) studied under the same conditions. We have checked that a 1 cm^2 Pt sheet or DSA grid immersed in ca. 100 mL electrochemical cell and polarized at ± 10 mA yielded FEs of 100% for HER and OER, respectively.

3 Results and Discussion.

3.1 Design of experiments (DOE).

3.1.1 Principle

The DOE approach is a formalism based on mathematics to simplify and rationalize scientific studies and to reduce the number of experiments without loss in the quality of conclusions.[33–35,37–39] It allows for multiple input experimental variables (factors) to be manipulated, determining their effect on a desired output (response). The simplest experimental design is the Hadamard array a^b which considers the effects of "b" factors set at "a" levels by the experimenter. It can benchmark and quantify the effect of numerous either quantitative or qualitative factors at two levels (named +1 or -1). If necessary, it can also be extended to then integrate supplementary factors in the DOE[40–43]. This experimental design dictates the experiments to be performed. The experimental data is then collected and processed using a statistical method based on the analysis of variance (ANOVA). It allows us to determine the probability for a factor or for an interaction between factors of having a significant influence on the response. The total variance consists of the variance of each factor and a residual variance. By comparison between the variance of the results for a factor and the residual variance, it is possible to determine an indicator named F. This value is then compared to a reference value F_{ref} extracted from the statistical Fisher-Snedecor table. We have considered F_{ref} values of 10.56 and 5.12 for 99 and 95% significance levels, respectively[44]. Consequently, the factor will be considered as influent at 99% probability if F > 10.56 and at 95% probability if F > 5.12.

In this work, we chose to use a 2^3 Hadamard matrix (Table 1) where factors 1, 2, and 3 are the compositions of the cathode and the anode, and the type of micropatterns engraved on the electrode, respectively (*vide supra*). This matrix also provides values for the effect a_i of a factor i (Eq. 1).

Table 1. 2^3 Hadamard Matrix for Three Factors F1 to F3 Set at Two Levels +1 and -1. FX/FY Represents the Interaction between Factors X and Y.

Run	F1	F2	F3	F1/F2	F1/F3	F2/F3	F1/F2/F3
1	+1	+1	+1	+1	+1	+1	+1
2	+1	+1	-1	+1	-1	-1	-1
3	+1	-1	+1	-1	+1	-1	-1
4	+1	-1	-1	-1	-1	+1	+1
5	-1	+1	+1	-1	-1	+1	-1
6	-1	+1	-1	-1	+1	-1	+1
7	-1	-1	+1	+1	-1	-1	+1
8	-1	-1	-1	+1	+1	+1	-1

$$a_i = \frac{1}{n}\left(\sum_{l=1}^{n} x_{i,l} y_l\right) (1)$$

Where n is the number of experiments contained in the DOE (here, n = 8); $x_{i,l}$ is the level of factor i (+1 or -1), referring to the experimental table (Table 1), for the experiment l; and y_l is the experimental value measured for the experiment l. For example, this gives for F1:

$$a_1 = \frac{1}{8}(y_1 + y_2 + y_3 + y_4 - y_5 - y_6 - y_7 - y_8) (2)$$

The effect a_i for a factor i is considered as influent only if it is higher than the value of the standard deviation of the experimental values from the DOE. The standard deviation at 68 % or 95 % can be retained depending on the desired accuracy. If the measured effect gives a positive value for a factor, and the objective is to decrease the value of the performance metric (e.g., overpotential for HER or OER, stability in operation), the level -1 of the factor in the DOE will have to be preferred.

3.1.2 Selection of the combinations cathode/anode from HER and OER half-reactions

In order to select the most promising combinations of cathode/anode which will be further included in the 2^3 Hadamard matrix, all the 25 cm^2 3D printed Ni-based binary alloyed materials, namely NiFe, NiCo, NiMo, and NiCr, were first examined for HER and OER half-reactions.

Before studying their electrocatalytic activity, the chemical composition and the homogeneity of these binary materials were determined by SEM-EDS at the micrometer scale. As reported in our previous study[32], NiCo showed a homogeneous distribution of Ni and Co elements with a Co content estimated at approximately 8% from EDS (Table S1). In contrast, Ni and Fe were not homogeneously distributed in NiFe and two phases were clearly visible, one majority phase incorporating μm-sized Fe particles in a Ni matrix and a second one with 20-30 μm-diameter Fe microparticles. The average Fe content was around 6%. The two newly prepared NiMo and NiCr electrodes also showed differences in the elemental homogeneity. Ni and Cr were homogeneously distributed in NiCr (Figure S2) with an overall composition estimated by EDS at 6% Cr and 70% Ni (Table S1). Similar to NiFe, NiMo consisted in a majority Ni-rich phase incorporating some areas of a few tens of μm of pure Mo (Figure S3). The average composition was found to be 3% for Mo and 71% for Ni. The phase segregation in this material could be reasonably explained by the large differences in the melting point of Mo and Ni, 2620°C and 1455°C, respectively. Indeed, SLM is a local process with fast heating and cooling times that can lead to some unavoidable inhomogeneities and the creation of defects[45,46].

Now, the electrocatalytic activity of the 25 cm^2 3D-printed electrodes was evaluated in alkaline medium (1.0 M KOH, pH 14) both for HER and OER. Considering the electrochemical surface area of these electrodes, it must be underlined that current intensities as high as 1 A could be reached. Ohmic drop-corrected cyclic voltammograms of the electrodes are shown in Figure 1 for HER and OER. NiCo, NiCr, and NiMo exhibited the highest HER activity, as supported by the lowest *iR*-corrected overpotential of 210 mV measured at 10 mA cm^{-2} (i.e. 250 mA) (Figure 1a). This value was 20 and 60 mV lower than those determined for reference Ni and NiFe, respectively (Table S2). Consistent with CV data, the charge-transfer resistance R_{ct} values measured at 100 mV overpotential for NiMo (136 mΩ cm^{-2}), NiCr (174 mΩ cm^{-2}) and NiCo (215 mΩ cm^{-2}) were smaller than those determined for Ni (280 mΩ cm^{-2}) and NiFe (454 mΩ cm^{-2}), demonstrating faster HER charge transfer kinetics (Table S2 and Figure S4). Interestingly, relatively close Tafel slopes were determined for all the studied electrodes, between ca. 90 and 105 mV per decade (Figure S5). Such values are indicative of a HER process controlled by the same reaction step, namely the Volmer reaction that corresponds to the adsorption of hydronium ions onto the active sites of the catalysts.

Regarding OER, NiFe and NiMo showed the lowest overpotentials at +10 mA cm^{-2} (300-310 mV, Table S3), when compared to NiCr (330 mV), Ni (350 mV), and NiCo (360 mV). Such a trend was also supported by the R_{ct} values increasing in the order: NiFe ≈ NiMo (6-10 mΩ cm^{-2}) < Ni (20 mΩ cm^{-2}) < NiCr (26 mΩ cm^{-2}) < NiCo (87 mΩ cm^{-2}) (Table S3 and Figure S4b). Moreover, the Tafel slopes measured for the binary alloys in the range of 33-50 mV per decade (Figure S5) were in perfect agreement with those determined for other Ni-based OER electrocatalysts[21,29,47].

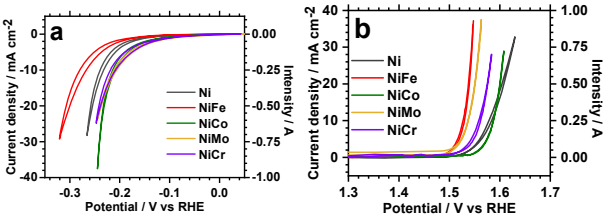

Figure 1. Ohmic-drop corrected cyclic voltammograms at 5 mV s^{-1} in KOH 1M of Ni, NiFe, NiCo, NiMo, and NiCr for HER (a) and OER (b).

Another essential performance indicator is the stability of the electrodes in operation. Long-term electrolytic tests were achieved at a constant current density of ±50 mA cm^{-2} over six days for HER and OER. The corresponding chronopotentiometric curves are shown in Figure 2. The NiCo, NiMo, and reference Ni electrodes were found to be

the most stable with a potential change of only 10 mV after 6 days of electrolysis, followed by NiCr (20 mV) and NiFe (40 mV) (Table S2). The Faradaic efficiency (FE) for HER was approximately 90%, as compared to a Pt reference electrode (Table S2). This value lower than 100% can be attributed to two factors: (*i*) the large size of the electrodes and the large headspace volume of the cell, which can lead to unavoidable loss of produced gas; and (*ii*) the increase in the temperature of the electrolytic solution by 7°C after electrolysis, which can also contribute to a reduced FE. Employed as anodes for OER, NiFe was the most robust electrode as its potential increased by only 30 mV over 6 days of electrolysis, followed by NiMo (70 mV), NiCr (80 mV), Ni (90 mV) and NiCo (100 mV) (Table S3). FE for OER was 100% vs reference DSA for all electrodes.

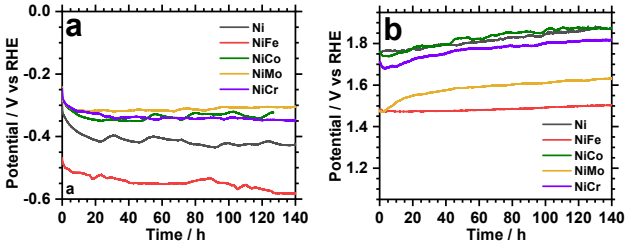

Figure 2. Chronopotentiometric curves for HER (a) and OER (b) of Ni, NiFe, NiCo, NiMo, and NiCr binary alloys at ±50 mA cm^{-2} in KOH 1M.

Post-electrolysis characterizations confirmed that the average metallic ratios of the electrodes remained almost unchanged after either HER or OER electrolysis (Table S1). Furthermore, EDS mapping showed the homogeneous distribution of metals in the post-electrolyzed binary alloys (Figure S6 and S7), except for NiMo. For the latter, it still exhibited inclusions of pure Mo in the Ni matrix after HER electrolysis (Figure S8) which disappeared after OER electrolysis (Figure S9) due to the Mo oxidation from 1 V vs RHE (Figure S10). Noticeably, the presence of potassium was systematically detected after the electrolytic tests, probably coming from the adsorption of potassium carbonates on the electrode surface. Such a result is consistent with the previous findings that Ni-based HER and OER electrocatalysts were routinely coated with this salt when polarized in alkaline KOH medium[15].

The analysis by ICP-AES of the electrolytic solution after HER electrolysis revealed no detectable levels of released metals whatever the tested electrode. In contrast, the OER electrolysis caused the release of metallic Ni from all electrodes at the level of traces, i.e 60-200 ppm. Moreover, Cr and Mo were also released from anodically polarized NiCr and NiMo, respectively, at contents corresponding to 0.6% and 0.9% of metal incorporated in their respective alloy. The release of Mo revealed by ICP-AES is consistent with the disappearance of patches of pure Mo observed by EDS mapping (Figure S9).

Based on the above results, we have considered NiCr (level +1) and NiCo (level -1) for the cathode (factor 1) of the full cell. NiMo (level -1) and NiFe (level +1) have been selected for the anode (factor 2) owing to their stability and their low overpotential as OER electrocatalysts. The micropatterns engraved on the 3D printed electrodes (factor 3) will be conical-shaped holes (level -1) and ramps (level +1) as such features have been demonstrated to be preferential sites for nucleation, growth, and release of the electrogenerated gas bubbles[48,49] (Figure S11). These were preferred to cylindrical micropatterns as they yielded more catalytically performing electrodes, as examplified for reference Ni (Figure S12). From profilometry and SEM measurements, the mean diameter and depth of the holes were estimated at 270 ± 50 μm and 55 ± 5 μm, respectively (Figures S13 and S14). Ramps had a Gaussian shape with 260 ± 50 μm height and 300 ± 10 μm width. Each pattern was separated by 2.50 ± 0.05 mm.

So, the 2^3 Hadamard matrix shown in Table 2 could be built by considering the three selected factors and their respective levels. Three key performance metrics (KPMs) characterizing the catalytic efficiency and the stability in operation of the electrodes were identified as response signals: *i*) the cell overvoltage determined by cyclic voltammetry at 10 mA cm^{-2} (η_{10}), *ii*) the cell overvoltage determined by chronopotentiometry after a 20 h electrolysis at 50 mA cm^{-2} (η_{50}) and *iii*) the voltage change caused by 120 h electrolysis at 50 mA cm^{-2}.

Table 2. 2^3 Hadamard Matrix for the Overall Water Electrolysis. Level +1: NiCr, NiFe, and ramps. Level -1: NiCo, NiMo and holes.

Run	F1 *Cathode*	F2 *Anode*	F3 *Pattern*
1	NiCr	NiFe	Ramps
2	NiCr	NiFe	Holes
3	NiCr	NiMo	Ramps
4	NiCr	NiMo	Holes
5	NiCo	NiFe	Ramps
6	NiCo	NiFe	Holes
7	NiCo	NiMo	Ramps
8	NiCo	NiMo	Holes
9 - Control	Ni	Ni	Ramps
10 - Control	Ni	Ni	Holes

3.2 Full cell measurements.

The overall water splitting was examined in alkaline medium (1M KOH, pH 14) using different combinations of cathode/anode/pattern, as defined in Table 2. Compared with reference Ni combinations, the binary alloyed ones exhibited overvoltages at 10 mA cm^{-2} lowered by 50 to 100 mV (Figure 3 and Table 3).

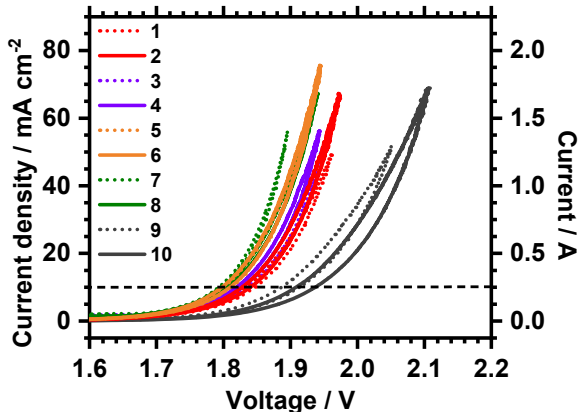

Figure 3. Cyclic voltammograms at 5 mV s^{-1} for overall water splitting in KOH 1M of different combinations cathode/anode/pattern: NiCr/NiFe (red, runs 1 and 2), NiCr/NiMo (purple, runs 3 and 4), NiCo/NiFe (orange, runs 5 and 6), NiCo/NiMo (green, runs 7 and 8) and Ni/Ni (grey, runs 9 and 10) covered by holes (solid lines) or ramps (dotted lines).

Table 3. Key Performance Metrics (KPMs) for Each Combination Cathode/Anode/Pattern Involved in the Overall Water Electrolysis.

Run	η_{10} / V[a]	η_{50} / V[b]	Electrolysis-induced voltage change / mV[c]
1	0.60	1.00	20
2	0.60	0.89	30
3	0.60	0.89	270
4	0.59	0.85	170
5	0.57	1.07	20
6	0.57	0.91	200
7	0.55	0.78	110
8	0.56	0.71	260
9 - Blank	0.68	1.18	110
10 - Blank	0.65	1.17	190

[a] Overvoltage (E_{10} – 1.23 V) determined by cyclic voltammetry at 10 mA cm^{-2}. [b] Overvoltage (E_{50} – 1.23 V) determined by chronopotentiometry after a 20 h electrolysis at 50 mA cm^{-2}. [c] After 120 h electrolysis at 50 mA cm^{-2}.

Full electrolysis cells exhibited low cell resistance (between 18 and 27 mΩ cm^{-2}) and based on η_{10} values, the combinations NiCo/NiMo incorporating ramps or holes were found to be the most performing ones.

Long-term electrolytic tests were then conducted over six days (140 h) at 50 mA cm^{-2} and the cell overvoltages after 20 h and 120 h of electrolysis were measured. As displayed in Figure 4 and consistent with CV data, NiCo/NiMo was still the most efficient combination as supported by the lowest η_{50} overvoltage of 0.71 or 0.78 V depending on whether the patterns were holes or ramps. η_{50} values in the range 0.85-1.00 V were determined for the other binary alloy electrodes. Despite higher catalytic efficiency, NiCo/NiMo was however less stable in operation when compared with the other combinations integrating NiFe as the anode (runs 1, 2, and 5). Indeed, the voltage change for NiCo/NiMo was higher than 110 mV after 120 h electrolysis, while the voltage was increased by only 20-30 mV for NiFe anodes (Table 3). It is also noticeworthy that these materials were still quite stable when current densities as high as 200 mA cm^{-2} were applied, as exemplified with the combination NiCo/NiMo/holes (Figure S15). Regarding the effect of the patterns, it is more difficult to rationalize. The introduction of holes would be beneficial to increase the catalytic efficiency of the electrodes, in terms of η_{10} and η_{50}, whereas ramps would yield more robust electrodes overall.

Compared with rare cutting edge studies related to overall water splitting from large-scale (> 10 cm^2) electrodes, our best performing 25 cm^2 electrodes were able to deliver current intensities exceeding 1 A at a cell voltage of ca. 2.0 V over at least one week. Such performance was globally superior to those reported by Yan et al. with nickel phosphides Ni_2P-Ni_5P_4-coated carbon cloth[50] and by Bui et al. with Ni-based electrodes[26]. Furthermore, our approach for fabricating 3D-printed functional electrodes is simpler and more direct than that used by Pumera and coworkers, and does not require a further surface functionalization step[30].

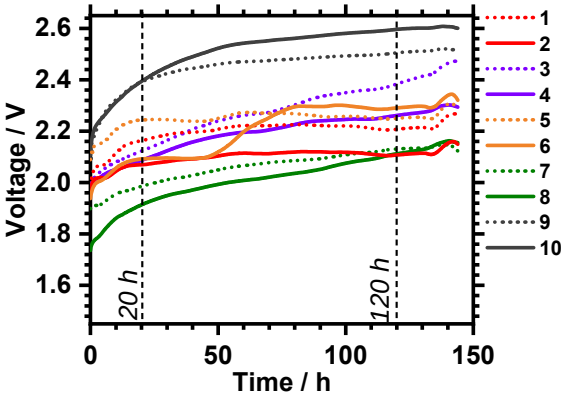

Figure 4. Cell voltage at 50 mA cm^{-2} for overall water splitting in KOH 1M of different combinations cathode/anode/pattern: NiCr/NiFe (red, runs 1 and 2), NiCr/NiMo (purple, runs 3 and 4), NiCo/NiFe (orange, runs 5 and 6), NiCo/NiMo (green, runs 7 and 8) and Ni/Ni (grey, runs 9 and 10) covered by holes (solid lines) or ramps (dotted lines).

3.3 Data analysis by the theory of design of experiments.

3.3.1 Analysis of Variance (ANOVA)

DOE theory allows to determine experimental work to quantify influence probability and effects for each considered factor. We first carried out an ANOVA for each selected KPM (Tables S4 to S6) and the variation of calculated F values is shown in Figure 5 as a function of the experimental factors and interactions between them. Two factors exhibited a clear influence with 99% probability: *i*) the composition of the cathode (NiCo or NiCr) on η_{10} and *ii*) the composition of the anode (NiFe or NiMo) on η_{50}. This last one could also be considered as influent on the voltage change caused by 120 h electrolysis at 50 mA cm^{-2} but with a probability level close to 95%.

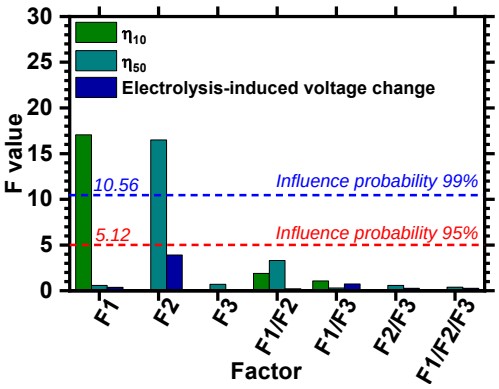

Figure 5. F values determined by ANOVA of three selected KPMs for three factors at two levels in the design of experiments. The Fisher-Snedecor factor values at 99 % and 95 % probabilities are 10.56 and 5.12, respectively. The factors 1, 2, and 3 are the compositions of the cathode and the anode, and the type of micropatterns engraved on the electrode, respectively. FX/FY corresponds to the interaction between factors X and Y.

3.3.2 Analysis of linear effects

The quantitative effects of each factor and interaction on the response signals (i.e. the KPMs) could be estimated using eq. 2. It is worth recalling that if the a_i value of the effect is superior to the standard deviation of measurements, the factor or interaction can be qualified as influent. For the first KPM, only the cathode composition (factor 1) exhibited a clear influence with a_1 equal to +18 mV (Figure 6). Therefore, it is recommended to select the level -1 of this factor, namely NiCo, to decrease η_{10} by 18 mV. This conclusion is in perfect line with trends observed from the electrochemical data (Figures 3 and 4) and ANOVA (Figure 5).

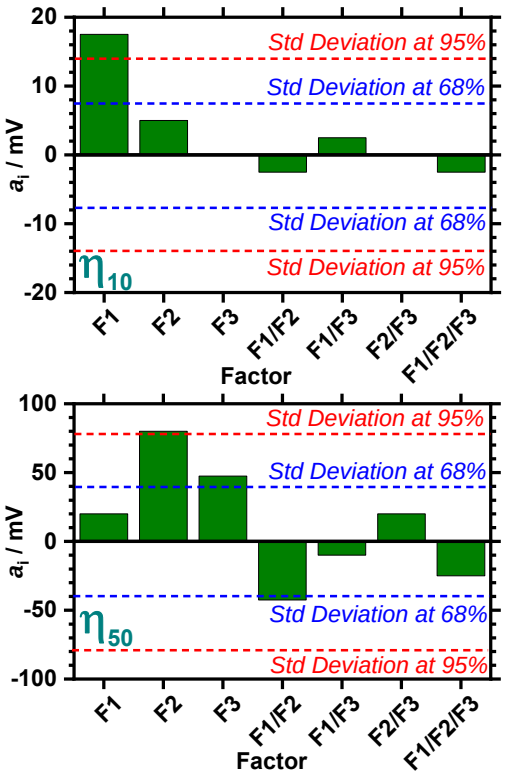

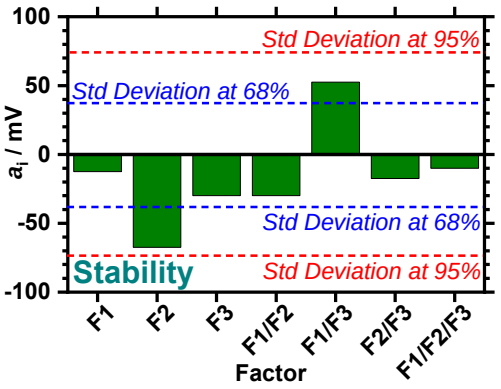

Figure 6. Estimation of the effect a_i of three factors on η_{10}, η_{50}, and the electrolysis-induced potential change. The factors 1, 2, and 3 are the compositions of the cathode and the anode, and the type of micropatterns engraved on the electrode, respectively. FX/FY corresponds to the interaction between factors X and Y.

Regarding the second KPM, the anode composition (factor 2) clearly played a key role in the measured overvoltage with an effect a_2 of +80 mV (Figure 6), which means that it is recommended to select the level -1 of this factor, namely NiMo, to decrease η_{50} by 80 mV. Surface pattern could also have a smaller influence on this second KPM. Its effet a_3 has been evaluated to be +48 mV which was higher than the standard deviation at 68 %. The level -1 of factor 3 should be consequently selected, i.e. holes, to decrease η_{50}. This is again consistent with data from Figures 3 to 5. Interestingly, the interaction between factors 1 (cathode composition) and 2 (anode composition) showed a significant effect a_{12} of -40 mV which was higher than the standard deviation at 68 %. This is consistent with the trend to prefer levels -1 of the cathode and anode to lower both η_{10} and η_{50}.

Finally, we analyzed the effect of the considered factors on the electrolysis-induced voltage change. The composition of the anode (factor 2) was found to be the single factor that almost reached the value of the standard deviation at 95% (Figure 6). The corresponding a_2 value was -68 mV which indicates that NiFe (level +1) should be preferred to improve the stability in operation of the cell. Such an assertion is somewhat opposite to that made from the factor effects on η_{50} for which NiMo anode was better to decrease η_{50}.

Conclusions

To conclude, we have produced novel self-supported 25 cm^2 3D-printed electrodes operating for overall water splitting in alkaline conditions at high current intensities (1.25 A). The originality of this work lies in the use of SLM 3D printing technology of metals to produce self-supported binary alloyed materials with novel shapes and surface micropatterns. This undoubtedly constitutes the most direct route to complex electrode structures, without any other step of surface functionalization. The preliminary study on the HER and OER half-reactions has enabled to select the best performing and robust electrodes for further full cell measurements. The DOE formalism has proved to be a valuable tool

to examine the effects of the cathode and anode compositions, but also the engraved patterns on some performance metrics (overvoltage and stability in operation) of the electrolysis cell. Our work perfectly demonstrates the power of DOE for energy-related studies to rationalize experiments and optimize performance with quantitative conclusions. It revealed that NiCo and NiMo should be preferentially used as the cathode and anode to decrease the cell overvoltage, whereas NiFe as the anode yielded the best stability in operation. This situation highlights the need for compromise between the factors to maximize the response signals. In that context, the introduction of Fe into the NiMo anode could be an interesting alternative. Besides, the impact of the micropatterns printed by SLM on the KPMs was limited, even though the presence of holes was rather beneficial for decreasing the cell overvoltage. It is obvious that the pattern resolution needs to be improved in the future to finely control the flow and release of electrogenerated gas bubbles in the electrolyzer.

As a first step towards the upscaling of our electrolyzer for the practical production of H_2, we have approximately calculated the consumed energy to produce 1 kg of H_2 using the combination NiCo/NiMo/holes as cathode/anode/pattern. An energy of 50.6 kWh was thus obtained, taking into account FE, cell voltage and the current intensity (Appendix S1). Although this value was extracted from a lab-scale electrolyzer, it was quite promising because it was slightly higher than the industrial target of 48 kWh set by the European Union for 2030[51].

ASSOCIATED CONTENT

Supporting Information. Photographs of the 3D printed electrodes, SEM images and EDS mapping, Nyquist and Tafel plots, supplementary chronopotentiometric curves, profilometry maps, the elemental composition of the electrodes determined by EDS before and after HER or OER electrolysis, key performance metrics for HER and OER, ANOVA tables for the three selected response signals, approximate calculation of the consumed energy to produce 1 kg of H_2. This material is available free of charge via the Internet at http://pubs.acs.org.

AUTHOR INFORMATION

Corresponding Author

* Loïc Perrin: loic.perrin@h2x-ecosystems.com
* Bruno Fabre: bruno.fabre@univ-rennes.fr

Author Contributions

B. F., L. P., and J. T. conceived the project and designed the experiments, J. T. performed experiments and analyzed the data. J. T. and B. F. wrote the manuscript. All authors contributed to the discussion of the results. All authors participated in editing the paper and have approved the final version of the manuscript. The SEM measurements have been performed on the CMEBA platform (ScanMAT, UAR 2025 University of Rennes-CNRS; CPER-FEDER 2015-2020). The authors declare no competing financial interest.

Funding Sources

ANRT (Agence Nationale de la Recherche Technologique) and H2X Ecosystems are acknowledged to fund this work through the CIFRE program.

Notes

Due to the industrial work, the SLM process laser parameters and Auto Desk Fusion instructions for the patterning of the electrodes are protected and under confidentiality for submitting further patents.

ACKNOWLEDGMENT

Axel Dubois and Hugo Schaal (CEO, SLS France) are fully acknowledged for their contribution to the fabrication of the 3D-printed electrodes. Loic Joanny is fully acknowledged for his contribution to SEM measurements. Muriel Escadeillas (CRMPO, Univ. Rennes) is fully acknowledged for ICP-AES measurements performed at CRMPO platform.

ABBREVIATIONS

ANOVA, Analysis Of Variance; AEM, Alkaline Exchange Membrane; AWE, Alkaline Water Electrolysis; DOE, Design Of Experiments; DSA, Double Stabilized Anode; EDS, Energy Dispersive X-Ray Spectroscopy; EIS, Electrochemical Impedance Spectroscopy; FE, Faradaic Efficiency; HER, Hydrogen Evolution Reaction; ICP-AES, Inductive Coupled Plasma Atomic Emission Spectroscopy; KPM, Key Performance Metric; OER, Oxygen Evolution Reaction; PEM, Proton exchange Membrane; SEM, Scanning Electron Microscopy; SLM, Selective Laser Melting.

REFERENCES

(1) Lewis, N. S.; Nocera, D. G. Powering the Planet: Chemical Challenges in Solar Energy Utilization. *Proc. Natl. Acad. Sci.* **2006**, *103* (43), 15729–15735.

(2) United States Department of Energy. A National Vision of America's Transition to a Hydrogen Economy - to 2030 and Beyond (Feb. 2002). https://www.ogel.org/article.asp?key=743.

(3) European Commission. Communication from the Commission to the European Parliament, the Council, the European Economic and Social Committee and the Committee of the Regions, 2020.

(4) Terlouw, T.; Bauer, C.; McKenna, R.; Mazzotti, M. Large-Scale Hydrogen Production *via* Water Electrolysis: A Techno-Economic and Environmental Assessment. *Energy Environ. Sci.* **2022**, *15* (9), 3583–3602.

(5) Kang, Y.; Cretu, O.; Kikkawa, J.; Kimoto, K.; Nara, H.; Nugraha, A. S.; Kawamoto, H.; Eguchi, M.; Liao, T.; Sun, Z.; Asahi, T.; Yamauchi, Y. Mesoporous Multimetallic Nanospheres with Exposed Highly Entropic Alloy Sites. *Nat. Commun.* **2023**, *14* (1), 4182.

(6) Jiang, B.; Guo, Y.; Sun, F.; Wang, S.; Kang, Y.; Xu, X.; Zhao, J.; You, J.; Eguchi, M.; Yamauchi, Y.; Li, H. Nanoarchitectonics of Metallene Materials for Electrocatalysis. *ACS Nano* **2023**, *17* (14), 13017–13043.

(7) International Energy Agency. The Future of Hydrogen, 2019.

(8) Cao, J.; Li, H.; Pu, J.; Zeng, S.; Liu, L.; Zhang, L.; Luo, F.; Ma, L.; Zhou, K.; Wei, Q. Hierarchical NiMo Alloy Microtubes on Nickel Foam as an Efficient Electrocatalyst for Hydrogen Evolution Reaction. *Int. J. Hydrog. Energy* **2019**, *44* (45), 24712–24718.

(9) Shiva Kumar, S.; Himabindu, V. Hydrogen Production by PEM Water Electrolysis – A Review. *Mater. Sci. Energy Technol.* **2019**, *2* (3), 442–454.

(10) Ehlers, J. C.; Feidenhans'l, A. A.; Therkildsen, K. T.; Larrazábal, G. O. Affordable Green Hydrogen from Alkaline

Water Electrolysis: Key Research Needs from an Industrial Perspective. *ACS Energy Lett.* **2023**, *8* (3), 1502–1509.
(11) Yu, Z.; Duan, Y.; Feng, X.; Yu, X.; Gao, M.; Yu, S. Clean and Affordable Hydrogen Fuel from Alkaline Water Splitting: Past, Recent Progress, and Future Prospects. *Adv. Mater.* **2021**, *33* (31), 2007100.
(12) Miller, H. A.; Bouzek, K.; Hnat, J.; Loos, S.; Bernäcker, C. I.; Weißgärber, T.; Röntzsch, L.; Meier-Haack, J. Green Hydrogen from Anion Exchange Membrane Water Electrolysis: A Review of Recent Developments in Critical Materials and Operating Conditions. *Sustain. Energy Fuels* **2020**, *4* (5), 2114–2133.
(13) Trasatti, S. Work Function, Electronegativity, and Electrochemical Behaviour of Metals. *J. Electroanal. Chem. Interfacial Electrochem.* **1972**, *39* (1), 163–184.
(14) Roger, I.; Shipman, M. A.; Symes, M. D. Earth-Abundant Catalysts for Electrochemical and Photoelectrochemical Water Splitting. *Nat. Rev. Chem.* **2017**, *1* (1).
(15) McCrory, C. C. L.; Jung, S.; Ferrer, I. M.; Chatman, S. M.; Peters, J. C.; Jaramillo, T. F. Benchmarking Hydrogen Evolving Reaction and Oxygen Evolving Reaction Electrocatalysts for Solar Water Splitting Devices. *J. Am. Chem. Soc.* **2015**, *137* (13), 4347–4357.
(16) McCrory, C. C. L.; Jung, S.; Peters, J. C.; Jaramillo, T. F. Benchmarking Heterogeneous Electrocatalysts for the Oxygen Evolution Reaction. *J. Am. Chem. Soc.* **2013**, *135* (45), 16977–16987.
(17) Callejas, J. F.; Read, C. G.; Roske, C. W.; Lewis, N. S.; Schaak, R. E. Synthesis, Characterization, and Properties of Metal Phosphide Catalysts for the Hydrogen-Evolution Reaction. *Chem. Mater.* **2016**, *28* (17), 6017–6044.
(18) Owens-Baird, B.; Kolen'ko, Y. V.; Kovnir, K. Structure–Activity Relationships for Pt-Free Metal Phosphide Hydrogen Evolution Electrocatalysts. *Chem. – Eur. J.* **2018**, *24* (29), 7298–7311.
(19) Babizhetskyy, V.; Kotur, B.; Oryshchyn, S.; Zheng, C.; Kneidinger, F.; Leber, L.; Simson, C.; Bauer, E.; Michor, H. Crystal and Electronic Structure and Physical Properties of Ni5P4. *Solid State Commun.* **2013**, *164*, 1–5.
(20) Zhang, Y.-C.; Han, C.; Gao, J.; Pan, L.; Wu, J.; Zhu, X.-D.; Zou, J.-J. NiCo-Based Electrocatalysts for the Alkaline Oxygen Evolution Reaction: A Review. *ACS Catal.* **2021**, *11*, 12485–12509.
(21) Zhang, W.; Li, D.; Zhang, L.; She, X.; Yang, D. NiFe-Based Nanostructures on Nickel Foam as Highly Efficiently Electrocatalysts for Oxygen and Hydrogen Evolution Reactions. *J. Energy Chem.* **2019**, *39*, 39–53.
(22) Jin, M.; Zhang, X.; Niu, S.; Wang, Q.; Huang, R.; Ling, R.; Huang, J.; Shi, R.; Amini, A.; Cheng, C. Strategies for Designing High-Performance Hydrogen Evolution Reaction Electrocatalysts at Large Current Densities above 1000 mA cm $^{-2}$. *ACS Nano* **2022**, *16* (8), 11577–11597.
(23) Gouvernement Castex. *Ordonnance Numéro 2021-167 Du 17 Février 2021 Relative à l'hydrogène*; 2021; Vol. JORF 42. https://www.legifrance.gouv.fr/jorf/id/JORFTEXT000043148001/.
(24) Ngo, T. D.; Kashani, A.; Imbalzano, G.; Nguyen, K. T. Q.; Hui, D. Additive Manufacturing (3D Printing): A Review of Materials, Methods, Applications and Challenges. *Compos. Part B Eng.* **2018**, *143*, 172–196.
(25) DebRoy, T.; Mukherjee, T.; Milewski, J. O.; Elmer, J. W.; Ribic, B.; Blecher, J. J.; Zhang, W. Scientific, Technological and Economic Issues in Metal Printing and Their Solutions. *Nat. Mater.* **2019**, *18* (10), 1026–1032.
(26) Bui, J. C.; Davis, J. T.; Esposito, D. V. 3D-Printed Electrodes for Membraneless Water Electrolysis. *Sustain. Energy Fuels* **2020**, *4* (4), 213–225.
(27) Esposito, D. V. Membraneless Electrolyzers for Low-Cost Hydrogen Production in a Renewable Energy Future. *Joule* **2017**, *1* (4), 651–658.
(28) Ambrosi, A.; Moo, J. G. S.; Pumera, M. Helical 3D-Printed Metal Electrodes as Custom-Shaped 3D Platform for Electrochemical Devices. *Adv. Funct. Mater.* **2016**, *26* (5), 698–703.
(29) Ambrosi, A.; Pumera, M. Multimaterial 3D-Printed Water Electrolyzer with Earth-Abundant Electrodeposited Catalysts. *ACS Sustain. Chem. Eng.* **2018**, *6* (12), 16968–16975.
(30) Browne, M. P.; Redondo, E.; Pumera, M. 3D Printing for Electrochemical Energy Applications. *Chem. Rev.* **2020**, *120* (5), 2783–2810.
(31) Lee, C.-Y.; Taylor, A. C.; Nattestad, A.; Beirne, S.; Wallace, G. G. 3D Printing for Electrocatalytic Applications. *Joule* **2019**, *3* (8), 1835–1849.
(32) Tourneur, J.; Joanny, L.; Perrin, L.; Paul, S.; Fabre, B. Efficient and Highly Stable 3D-Printed NiFe and NiCo Bifunctional Electrodes for Practical HER and OER. *ACS Appl. Eng. Mater.* **2023**, *1* (10), 2676–2684.
(33) Goupy, J. *La Méthode Des Plans d'Expériences*, 2nd ed.; Dunod, 1996.
(34) Pillet, M. *Les Plans d'Expériences Par La Méthode Taguchi*; Organisation, 1997.
(35) Sabre, R. *Plans d'Expériences - Méthode de Taguchi*; Techniques de l'Ingénieur, 2007, 17.
(36) Kawashima, K.; Márquez, R. A.; Son, Y. J.; Guo, C.; Vaidyula, R. R.; Smith, L. A.; Chukwuneke, C. E.; Mullins, C. B. Accurate Potentials of Hg/HgO Electrodes: Practical Parameters for Reporting Alkaline Water Electrolysis Overpotentials. *ACS Catal.* **2023**, *13* (3), 1893–1898.
(37) Goupy, J. *Plans d'Expériences : Les Mélanges*; Dunod, 2001.
(38) Goupy, J. *Plans d'Expériences*, Techniques de l'Ingénieur, 1997, 1.
(39) Goupy, J.; Creighton, L. *Introduction Aux Plans d'Expériences, 3rd ed.*; Dunod, 2006.
(40) Park, G.-J. *Analytical Methods for Design Practice*, 1st ed.; Springer London, 2007.
(41) Eriksson, L. *Design of Experiments, Principles and Applications*, 3rd ed.; Umetrics Academy, 2000.
(42) Lee, R. Statistical Design of Experiments for Screening and Optimization. *Chem. Ing. Tech.* **2019**, *91* (3), 191–200.
(43) Draper, N. R.; Pukelsheim, F. An Overview of Design of Experiments. *Stat. Pap.* **1996**, *37* (1), 1–32.
(44) Poirier, J. Tables Statistiques. *Tech. Ing.* **1992**.
(45) Wang, Y.; Li, R.; Niu, P.; Zhang, Z.; Yuan, T.; Yuan, J.; Li, K. Microstructures and Properties of Equimolar AlCoCrCuFeNi High-Entropy Alloy Additively Manufactured by Selective Laser Melting. *Intermetallics* **2020**, *120*, 106746.
(46) Chiocca, A. Etude de l'influence Des Écoulements Dans Le Bain de Fusion Sur Les Mécanismes de Solidification En Cours de Soudage Sur l'alliage $Cu_{30}Ni$, Montpellier, 2016.
(47) Yu, M.; Budiyanto, E.; Tüysüz, H. Principles of Water Electrolysis and Recent Progress in Cobalt-, Nickel-, and Iron-Based Oxides for the Oxygen Evolution Reaction. *Angew. Chem. Int. Ed.* **2022**, *61* (1), e202103824.
(48) Zhang, F.; Ji, R.; Liu, Y.; Pan, Y.; Cai, B.; Li, Z.; Liu, Z.; Lu, S.; Wang, Y.; Jin, H.; Ma, C.; Wu, X. A Novel Nickel-Based Honeycomb Electrode with Microtapered Holes and Abundant Multivacancies for Highly Efficient Overall Water Splitting. *Appl. Catal. B Environ.* **2020**, *276*, 119141.

(49) Bintein, P.-B.; Lhuissier, H.; Mongruel, A.; Royon, L.; Beysens, D. Grooves Accelerate Dew Shedding. *Phys. Rev. Lett.* **2019**, *122* (9), 098005.
(50) Yan, Y.; Lin, J.; Bao, K.; Xu, T.; Qi, J.; Cao, J.; Zhong, Z.; Fei, W.; Feng, J. Free-Standing Porous Ni2P-Ni5P4 Heterostructured Arrays for Efficient Electrocatalytic Water Splitting. *J. Colloid Interface Sci.* **2019**, *552*, 332–336.
(51) European Energy Research Alliance. *Key Performance Indicators (KPIS) for FCH Research and Innovation, 2020 - 2030*; European Energy research Alliance.

Table of Contents artwork